

Neural Networks Based Sea Ice Detection and Concentration Retrieval From GNSS-R Delay-Doppler Maps

Qingyun Yan, *Student Member, IEEE*, Weimin Huang, *Senior Member, IEEE*, and Cecilia Moloney, *Member, IEEE*

Abstract—In this paper, a neural networks (NN) based scheme is presented for detecting sea ice and retrieving sea ice concentration (SIC) from global navigation satellite system reflectometry delay-Doppler maps (DDMs). Here, a multilayer perceptron neural network with back-propagation learning is adopted. In practice, two NN were separately developed for sea ice detection and concentration retrieval purposes. In the training phase, DDM pixels were employed as an input. The SIC data obtained by Nimbus-7 SMMR and DMSP SSM/I-SSMIS sensors were used as the target data, which were also regarded as ground-truth data in this paper. After the training process using a dataset collected around February 4, 2015, these networks were used to produce corresponding detection and concentration estimation for other four sets of DDM data, which were collected around February 12, 2015, February 20, 2015, March 16, 2015, and April 17, 2015, respectively. Results show high accuracy in sea ice detection and concentration estimation with DDMs using the proposed scheme. On average, the accuracy for sea ice detection is about 98.4%. In terms of estimated SIC, the mean absolute error is less than 9%, whereas the correlation coefficient is as high as 0.93 compared with the reference data. It was also found that low sea state and wind speed could lead to an overestimation of SIC for partially ice-covered region.

Index Terms—Back-propagation learning, delay-Doppler map (DDM), global navigation satellite system reflectometry (GNSS-R), neural networks (NN), sea ice concentration (SIC).

I. INTRODUCTION

A GOOD knowledge of sea ice conditions is critical for climate studies since global extrapolations of surface energy flux are highly sensitive to the estimates of total ice cover in the Arctic [1]. In addition, sea ice has a significant impact on the human activities, such as offshore oil and gas development [2] and the global shipping industries [3]. Compared with in situ monitoring, remote sensing technology offers an exciting alternative method for obtaining sea ice data that is both efficient and cost effective. For sea ice observations, there are three general remote sensing systems, which are based on sensors operating

at visible, near-infrared, and microwave bands, respectively [4]. These approaches exhibit characteristic advantages as well as weaknesses with respect to their resolution, functionality, and accuracy. As the performance among different kinds of sensors varies across surfaces of different types and conditions, employing multiple sensors allows us to compensate for some deficiencies of one sensor with the strengths of another [5]. Therefore, it is important to have multiple instruments to fulfill sea ice remote sensing so that the results can be more accurate and cost efficient.

Recently, global navigation satellite system reflectometry (GNSS-R) has appeared as an emerging remote sensing tool. The use of GNSS-R signals for sea ice sensing was initially demonstrated by Komjathy *et al.* [6]. Following this, sea ice remote sensing using GNSS-R has been carried out from land-based [7], [8], airborne [9], and spaceborne [10] instruments. With the launch of TechDemoSat-1 (TDS-1) mission more than 1 million delay-Doppler maps (DDMs) have been made public, which facilitates the study of sea ice sensing using DDMs. In [11], the feasibility of identifying the edges of sea ice was investigated. In 2015, Peraza *et al.* attempted to relate DDM features to ice conditions [12]. More recently, high accuracy in sea ice detection has been obtained using DDM observables (features extracted from DDMs) [13], [14] or through investigating the degree of coherence of the waveform extracted from DDM [15].

The technique of neural networks (NN) has been identified as a robust candidate for improving existing sea ice remote sensing applications [5], because the NN is able to approximate large varieties of functions without *a priori* assumption about their distribution, and to develop decision surfaces of any configuration using a learning process [16]. The NN-based sea ice remote sensing has already shown great potential with many different types of data (e.g., SAR images [17] and passive microwave data [18]). However, to the authors' knowledge, there is no research addressing NN-based sea ice remote sensing using GNSS-R DDMs.

In this paper, the technique of NN is applied to DDMs, for the first time, for the purposes of detecting sea ice and estimating sea ice concentration (SIC, which is defined as the ratio of coverage area by sea ice to seawater within a given region). Here, a multilayer perceptron (MLP) NN is developed and applied to the DDM data extracted from TDS-1 mission. This paper is organized as follows. Section II introduces the study area and

Manuscript received January 20, 2017; revised March 3, 2017; accepted March 27, 2017. Date of publication April 17, 2017; date of current version August 9, 2017. This work of W. Huang was supported by the Natural Sciences and Engineering Research Council of Canada under Grant NSERC 402313-2012. (Corresponding author: Weimin Huang.)

The authors are with the Faculty of Engineering and Applied Science, Memorial University, St. John's, NL A1B 3X5, Canada (e-mail: qy2543@mun.ca; weimin@mun.ca; cmoloney@mun.ca).

Color versions of one or more of the figures in this paper are available online at <http://ieeexplore.ieee.org>.

Digital Object Identifier 10.1109/JSTARS.2017.2689009

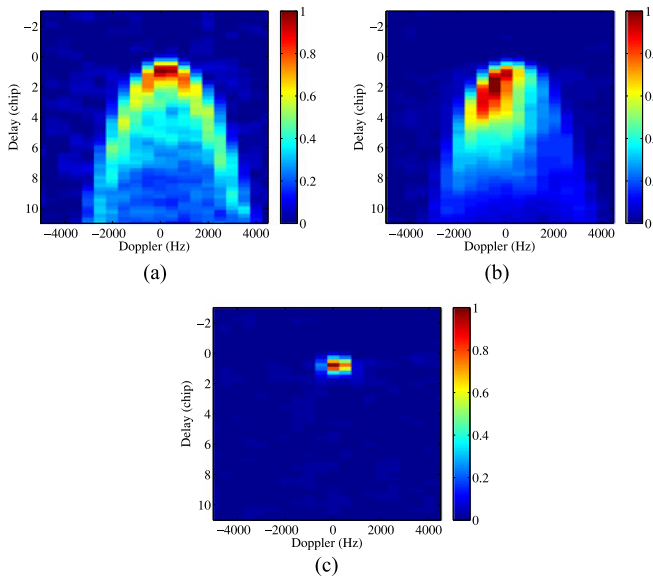


Fig. 1. GNSS-R DDMs collected by TDS-1 over regions with different SICs: (a) 0%, (b) 50%, and (c) 92%, respectively. All DDMs have been normalized with power values from 0 to 1.

the employed datasets. The proposed NN-based sea ice remote sensing scheme is described in Section III. Results are presented in Section IV, followed by conclusions in Section V.

II. DATA DESCRIPTION

A. Spaceborne GNSS-R DDM Data

DDM data collected in five periods 3–5 (RD 17), 11–13 (RD 18), and 19–21 (RD 19) in February, 15–17 (RD 23) in March, and 16–18 (RD 27) in April, 2015 around the Arctic regions by TDS-1 (available on www.merrbys.co.uk) are employed in this study. Details of the TDS-1 DDM data can be found in [19] and [20]. The DDM metadata also provides the specular point (SP) position for each DDM. Here, the SP is regarded as the location of a DDM. Such information can be utilized to extract the collocated SIC from the reference data that is described in the Section II-A. In addition, the signal-to-noise ratio (SNR) at the peak power point is also available and employed for data quality control.

Examples of the GNSS-R DDMs collected by TDS-1 over the regions with different SIC values (0%, 50%, and 92%, respectively) are shown in Fig. 1. The SIC values were obtained from the reference data for corresponding SP position of each DDM. From Fig. 1, the differences among DDMs over varying surface conditions are obvious. As the SIC values increase, the associated DDMs become less spread. It should be noted that each delay chip consists of four bins and the Doppler resolution is 500 Hz.

B. Ground-Truth Data

The reference SIC data employed in this paper are derived from that collected by multiple sensors: the scanning multichannel microwave radiometer (SMMR, carried aboard Nimbus-7),

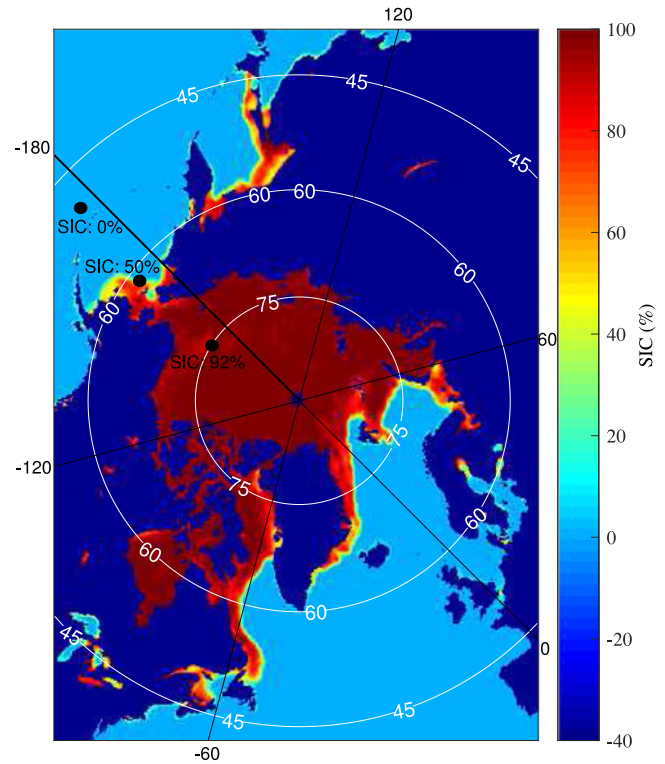


Fig. 2. Example of the daily SIC modified from [21]. The SIC value is from 0 to 100 (%). The land and the region without data is marked by dark blue (with a value of -40) for illustration purposes. White circles and black straight lines represent the latitudes and longitudes (in degree), respectively. The black circular areas (with a radius of about 100 km) indicate the approximate glisting zones of DDMs in Fig. 1.

the special sensor microwave/imagers (SSM/Is) on the defense meteorological satellite program (DMSP) -F8, -F11, and -F13 satellites, and the special sensor microwave imager/sounder (SSMIS) on the DMSP-F17 satellite [21]. These data provide daily and monthly averaged SIC for both the northern and southern hemispheres with different spatial coverage and have been valuable sources for global sea ice studies. This paper focuses on the SIC analysis in the northern hemisphere. The corresponding data are stored as images each with a size of $448 \text{ rows} \times 304 \text{ columns}$. In addition, the resolution for each grid is about $25 \times 25 \text{ km}^2$. The data values range from 0 to 255, in which $[0, 250]$ represent valid SIC values and the rest indicates land information or missing data. For better illustrations, the SIC value is multiplied by 0.4 (which thus falls in $[0, 100]$ in percentage) and the original data with value greater than 250 are set as -40 . An example of the rescaled data for February 4, 2015 is shown in Fig. 2.

III. DESIGN OF NN-BASED SEA ICE REMOTE SENSING

An NN devises a structure for complex data processing using information-processing units, also known as neurons. Typically, a network consists of the input layer, one or more hidden layers, and an output layer. The adjacent layers are connected by activation functions parameterized by weights. The activation functions are usually predefined and the weights are determined

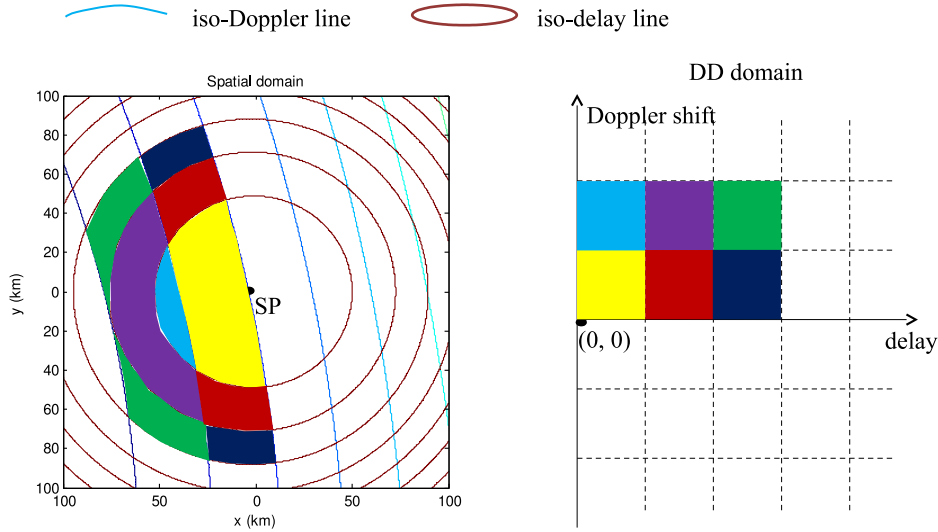


Fig. 3. Relationship between spatial clusters and DDM pixel. The same color indicates the association between the spatial clusters and DDM pixel. For concision, only selected pairs have been demonstrated.

through a training process. Consequently, a trained network can be regarded as an input–output mapping [22].

A GNSS-R DDM depicts the scattered power off the observed surface. The received signal can be considered as a superposition of scattering components from different points on the observed surface. Each component has its corresponding delay and Doppler shift (which are caused by different path lengths and the relative motions of the transmitter, the receiver, and the scattering point, respectively). Accordingly, each DDM pixel is associated with the scattering strength off corresponding clusters in the spatial domain and the relationship is shown in a concise form, as shown in Fig. 3.

Therefore, the surface scattering properties (for example, roughness) can be interpreted based on a DDM. In remote sensing area, it is well known that the scattering characteristics of sea ice and seawater differ from each other. Correspondingly, the DDMs of seawater and sea ice surfaces will be distinct. In addition, it is believed that the ratio of sea ice to seawater (i.e., SIC) within the region of interest will affect the DDMs (see Fig. 1). As such, the sea ice remote sensing from DDMs is feasible and investigated using the NN technique here. The general NN procedure for the application here consists of three steps: preprocessing of the input (DDM, in this study) data, training of the NN, and the estimation of ice information from another set of data using the trained NN.

A. DDM Data Preprocessing

Each measured DDM is processed with

- 1) noise floor subtraction;
- 2) normalization;
- 3) signal box determination; and
- 4) data stretching.

1) *Noise Floor Subtraction*: To reduce the effect of noise fluctuation due to antenna and instrument system noise variation, the noise floor is first subtracted from each DDM, which

can be calculated using the following expression:

$$\text{Noise} = \frac{1}{X} \sum_{\tau=\tau_1}^{\tau_2} \sum_{f=f_1}^{f_2} \text{DDM}(\tau, f) \quad (1)$$

where τ_1 , τ_2 , f_1 , and f_2 are the pixel limits of a noise box in the signal-free DDM area, and X is the number of pixels within the noise box. following [19], the noise box is chosen as the DDM area of the first four available delay rows spanning all Doppler bins (20) to ensure the absence of actual DDM signal within the noise box. The process mentioned above is a typical technique to deal with thermal noise. For speckle noise, it can be reduced through incoherent processing of GNSS-R signals. It is worth mentioning that TDS-1 DDMs have already been processed with 1 s (1000 looks) incoherent summation. The speckle noise can be further reduced by additional incoherent summation of the DDMs. However, the incoherent summation process will reduce the spatial resolution. In order to preserve the maximal achievable spatial resolution of TDS-1 DDM, no further incoherent summation is applied in this paper.

2) *Normalization*: After the noise level subtraction, DDM is normalized with respect to its peak power. The peak power point is determined through extracting the local maxima in the DDM [19].

3) *Signal Box Determination*: Consequently, the signal box is chosen based on the delay bin of the peak power point (bin_τ). Here, 40 bins in delay axis (from $\text{bin}_\tau - 4$ to $\text{bin}_\tau + 35$) and all the 20 bins in Doppler axis are retained. It should be noted that the size of the signal box corresponds to a spatial coverage between 100 and 150 km (median value 125 km) depending on the elevation angle at the SP.

4) *Data Stretching*: As the input layer of an NN is in the form of one-dimensional (1-D) vector. Thus, the 2-D DDM needs to be stretched. For each signal box, the DDM is sliced along the delay-axis, forming a 1-D vector with 800 elements. It is worth mentioning that the DDM can be sliced along either the delay- or the Doppler-axis. However, once one manner is chosen, the

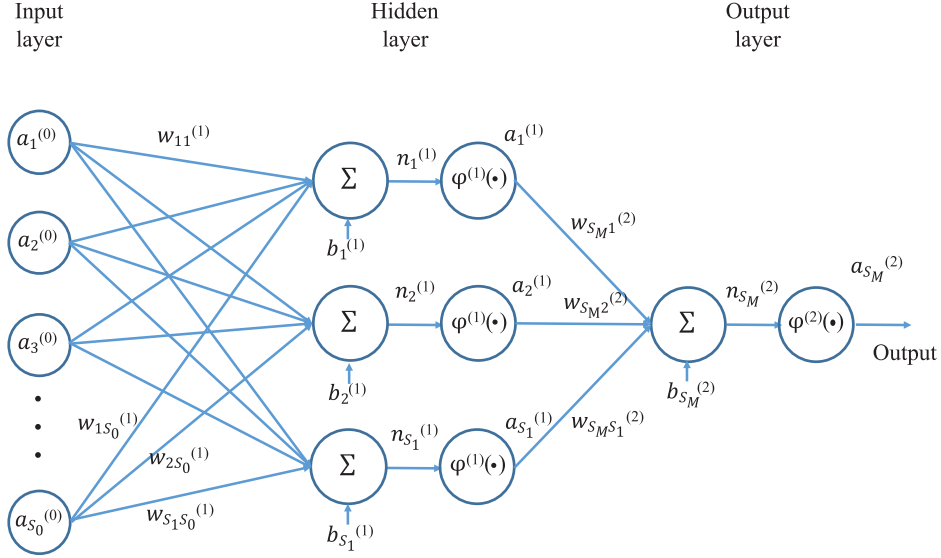


Fig. 4. Diagram of a three-layer MLP.

rest DDMs should be addressed in the same fashion, so that all the DDM pixels can be presented to the network in an orderly form.

B. Data Quality Control and Modification

In this paper, DDM samples with SNR (at peak power point) lower than 0 dB (which means the peak power value is even below the noise level) were rejected. To minimize the effect of scattering off lands, the DDMs with SPs over land and near coastal lines (within 50 km) were manually filtered out as well.

It should be noted that the coverage area corresponding to the DDM signal box is about $125 \times 125 \text{ km}^2$ while the grid size is of $25 \times 25 \text{ km}^2$ for the original SIC reference data. In order to match the coverage area of the DDM signal box, every SIC value in the original reference data was averaged by its surrounding 5×5 grids. Specifically, each grid with a valid SIC value (from 0 to 100) was averaged by those (also valid) within its surrounding 5×5 grids.

After the averaging, the associated SIC value were extracted according to the SP location of each DDM, and normalized to 1. For ice detection application, a threshold of 0.15 used in [23] is applied to the extracted SIC data. A data grid with an SIC value greater than 0.15 will be regarded as “ice covered” and assigned with 1, otherwise, 0.

C. NN Design

1) *NN Structure*: As pointed out in [24], an MLP with a single hidden layer is capable of approximating any continuous multivariate function to desired accuracy. Thus, an MLP was employed here (see Fig. 4) and was constructed with 800 inputs, 1 hidden layer consisting of 3 neurons, and 1 output. With reference to Fig. 4, $M = 2$ (the number of layers is $M + 1$), the number of inputs $S_0 = 800$, the number of hidden neurons $S_1 = 3$, and the number of output $S_M = S_2 = 1$. Through experiment, it was found that the accuracy was insensitive to the

increase in S_1 , whereas the computational time increased significantly. Hence, $S_1 = 3$ was selected by considering plausible performance in both accuracy and computational cost.

The DDM pixels from each DDM image will be presented to the input layer, as $a_l^{(0)}$, $l \in [1, 800]$ and the output will be SIC value (or, 0 or 1 for ice detection application), as $a_1^{(2)}$. More generally, the net input to neuron j in layer $k + 1$ can be described by $n_j^{(k+1)}$ and the corresponding output will be $a_j^{(k+1)}$. In Fig. 4, S_k is the number of neurons in layer k , $w_{ji}^{(k+1)}$ represents the synaptic weights connecting neuron j in layer $k + 1$ and neuron i in layer k and $\varphi^{(k+1)}(\cdot)$ and $b_j^{(k+1)}$ denote the activation function and bias for neuron j in layer $k + 1$, respectively. To be concise, not all weights are presented for the designed three-layer network in Fig. 4.

The relationship within the network can be given in the following concise matrix form:

$$\mathbf{a}^{(0)} = \mathbf{p} \quad (2)$$

$$\mathbf{a}^{(k+1)} = \varphi^{(k+1)}(\mathbf{W}^{(k+1)}\mathbf{a}^{(k)} + \mathbf{b}^{(k+1)}), k \in [0, 1] \quad (3)$$

where \mathbf{p} is the input DDM pixels vector and $\mathbf{a}^{(k+1)}$, $\mathbf{b}^{(k+1)}$, and $\mathbf{W}^{(k+1)}$ represent the input vector, the bias vector, and the weight matrix, respectively.

The activation functions in the hidden and the output layers were given separately by the widely used sigmoid function $\varphi^{(1)}(x) = 1/(1 + e^{-x})$ and the linear function $\varphi^{(2)}(x) = x$.

2) *Back-Propagation Learning*: The back-propagation learning [25] is a computationally efficient method for determining the weights [22]. This learning method consists of two passes through the different layers of the network: A forward pass and a backward pass. The forward pass can be summarized by (2) and (3), during which the weights in the network are all fixed. During the backward pass, on the other hand, the weights are all adjusted based on the sum of squared error, which is

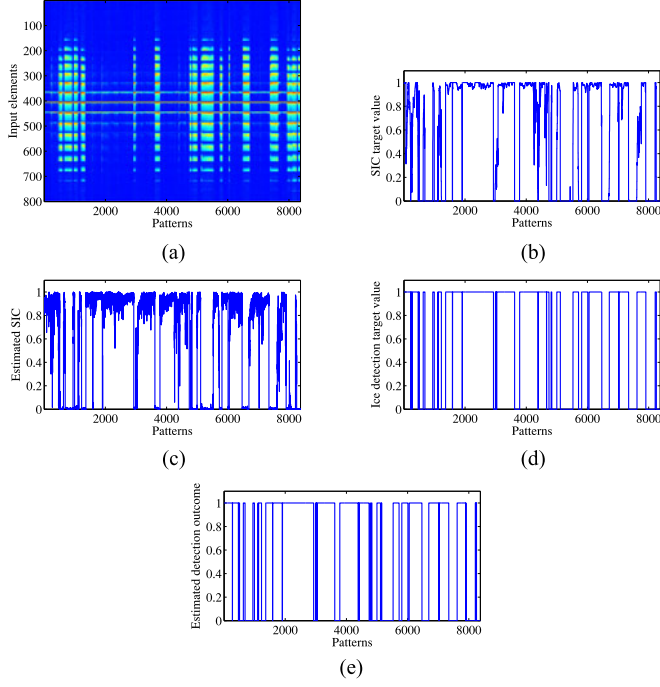


Fig. 5. 8377 training samples presented to the NN: (a) input vectors (each vertical slice is one vector), (b) target output for SIC estimation, (c) estimated SIC, (d) desired output for ice detection, and (e) estimated detection outcome.

defined as

$$\varepsilon = \frac{1}{2} \sum_{q=1}^Q \mathbf{e}(q)^T \mathbf{e}(q) \quad (4)$$

where $\mathbf{e}(q) = \mathbf{t}(q) - \mathbf{a}^{(2)}(q)$ is the error for the q th input and Q is the number of input patterns, and $\mathbf{a}^{(2)}(q)$ and $\mathbf{t}(q)$ are, respectively, the actual and the desired output SIC values (or ice labeling values) when the q th input $\mathbf{p}(q)$ is presented. The back-propagation learning aims at minimizing ε through adjusting weights. Among different algorithms for back-propagation learning, the Levenberg–Marquardt (LM) algorithm [26] is regarded as one of the most efficient algorithms, which allows fast and stable convergence for networks with a few hundred weights [27], [28]. The LM algorithm was employed to optimize ε by iteratively updating the weight vector \mathbf{m} in the following manner:

$$\text{new } \mathbf{m} = \mathbf{m} - (\mathbf{J}^T \mathbf{J} + \mu \mathbf{I})^{-1} \mathbf{J}^T \mathbf{e} \quad (5)$$

where $\mathbf{m} = [w_{11}^{(1)} w_{12}^{(1)} \dots w_{S_1 S_0}^{(1)} b_1^{(1)} \dots b_{S_1}^{(1)} w_{11}^{(2)} \dots w_{S_M}^{(2)} \dots b_{S_M}^{(M)}]^T$ (that consists of all the weights and biases in each layer), μ is the combination coefficient, \mathbf{I} is the identity matrix. \mathbf{e} contains the error for all Q input patterns, and $\mathbf{J} = \partial \mathbf{e} / \partial \mathbf{m}$ is the Jacobian matrix (see more details in [22], [27], and [28]).

In summary, the LM algorithm based back-propagation learning is implemented as follows.

- 1) Initialize \mathbf{m} (or equivalently, \mathbf{W} and \mathbf{b}) with random numbers, $\mu = 0.01$ and the multiplication factor $\beta = 10$ (according to [27]) and present all input patterns to the network.

TABLE I
DATA EMPLOYED IN THIS PAPER

Training			Testing						
RD 17			RD 18		RD 19	RD 23		RD 27	
0014	0021	0024	0000	0007	0021	0036	0020	0043	0053
0026	0027	0051	0008	0012	0096	0098	0025	0109	0193
0062	0064	0108	0016	0051	0135	0137	0074	0194	0198
0113	0119	0158	0060	0062	0142	0147	0076	0293	0294
0159	0163	0167	0128	0134	0179	0212	0118	0297	0300
0169	0194	0202	0164	0169	0217	0221	0119	0340	0343
0203	0213	0256	0170	0180	0263	0268	0153	0387	0397
0260	0261	0301	0245	0288	0269	0270	0156	0399	0440
0305	0341	0344	0290	0296	0302	0315	0162	0444	0445
0345	0370	0372	0297	0339	0316	0317	0237	0479	0484
0385	0389	0435	0346	0350	0353	0497	0241	0488	0543
0444	0478	0480	0355	0389	0571	0578	0244	0546	0576
0482	0517	0521	0395	0405	0584	0586	0285	0580	0581
0528	0603	0606	0406	0455	0622	0625	0293	0585	0619
0612	0615	0616	0457	0460	0659	0661	0326	0628	0630
0617	0618	0653	0505	0506	0666	0710	0337	0662	0666
0654	0655	0695	0551	0552	0745	0747	0338	0668	0731
0700	0725	0732	0555	0615	0750	0751	0339	0736	0741
0736	0766	0767	0646	0651	0754	0789	0378	0892	0940
0773	0830	0873	0652	0657	0793	0832	0423	0993	0996
0885	0931	0934	0659	0681	0839	0888	0427	0998	1001
0935	0966	0974	0682	0691	0891	0897	0428	1003	1040
0986	0988	1035	0692	0730	0932	0933	0457	1049	1086
1038	1039	1040	0770	0771	0945	0975	0462	1090	1092
1073	1077	1078	0774	0805	0981	0993	0463	1131	1226
1081	1116	1121	0806	0815	1044	1120	0467	1230	1269
1125	1126	1127	0863	0865	1129	1211	0547	1276	1314
1130	1168	1173	0869	0871	1240	1245	0548	1317	1320
1178	1179	1217	0873	0904	1246	1250	0555	1358	1361
1222			0911	0912	1252		0684	1364	1367

Note: Each four digits represent track ID. With both track ID and receiver data (RD) number, one DDM dataset can be Identified.

- 2) Proceed forward pass and compute the sum square error using (2)–(4).
- 3) Derive the Jacobian matrix \mathbf{J} .
- 4) Update \mathbf{m} using (5). Recompute the sum square error with new \mathbf{m} . If the new ε is smaller than the previous one, retain the updated \mathbf{m} , decrease μ by β and go to step 2. Otherwise, keep the previous \mathbf{m} , increase μ by β and repeat this step.
- 5) This learning process stops when any of the following occurs (numbers in brackets were empirically employed for this paper).
 - a) The preset maximum number (1000) of iterations is reached.
 - b) μ exceeds the preset threshold (10^{10}).
 - c) ε is below the required value (0.01).

IV. RESULTS

A. Training Results

The training was implemented using the data collected from February 3 to 5, 2015. The processed DDM data were regarded as inputs and associated ice data from SMMR and DMSP SSM/I-SSMIS Passive Microwave sensors were treated as desired output. The number of training patterns was 8377. The patterns (input and two different target outputs) along with the

TABLE II
ERROR STATISTICS FOR ICE DETECTION AND SIC RETRIEVAL

ID	Collection Period	No. of Employed DDMs	Ice detection		SIC retrieval			
			Errors No./Accuracy	Errors No. Using [14]/Accuracy	E_{av}	E_{abs}	E_{std}	R
RD 17 (training)	February 3–5, 2015	8377	80/99.05%	171/97.96%	0.00	0.06	0.11	0.97
RD 18 (test)	February 11–13, 2015	6071	92/98.48%	111/98.17%	−0.01	0.10	0.17	0.91
RD 19 (test)	February 19–21, 2015	4915	114/97.68%	168/96.58%	−0.02	0.10	0.16	0.93
RD 23 (test)	March 15–17, 2015	4799	98/97.96%	112/97.67%	−0.02	0.07	0.13	0.95
RD 27 (test)	April 16–18, 2015	8522	136/98.40%	162/98.10%	0.00	0.11	0.18	0.90

corresponding estimation are illustrated in Fig. 5. It should be mentioned that each vertical slice (with 800 elements) in Fig. 5(a) is one input vector and the horizontal axis denotes the sample sequence. The corresponding target SIC value and ice detection outcome are presented in Fig. 5(b) and (d) and the associated estimation are shown in Fig. 5(c) and (e), respectively. As shown in Fig. 5(a), some of the vertical slices are more stretching and they usually correspond to low values in reference SIC data. Typically, such slices are extracted from DDMs of seawater as these DDMs are usually more spread compared with the DDMs of sea ice [14] (also see Fig. 1). As pointed out in [9], at L-band the ice-covered sea surface can be described as a semitransparent layer of sea ice bound by seawater underneath. The scattering will be dominated by the lowermost seawater boundary if the sea ice thickness is lower than penetration depth (at L-band, the penetration depth in saline ice can be up to 2 m but more for freshwater ice [29]). It is also believed that the ice–water interface can be treated as a smooth surface [30]. Hence, a DDM collected over a fully (or almost fully) ice-covered region is usually associated with a mirror-like reflection from a nearly flat surface. As a result, only the region immediate around the SP is able to redirect the incoming signals toward the receiver. Correspondingly, the DDM [see Fig. 1(c)] appears similar to the clean Woodward Ambiguity Function (WAF). As has been found in [15], the more the DDM resembles WAF, the more coherent the scattering is, and the possibility of a flat ice surface being involved is higher. Instead, roughness of open oceans can vary considerably, but can still be assumed to be rougher than ice [14]. Therefore, nonspecular regions of the ocean corresponding to delay-Doppler offsets are more likely to reflect a GNSS signal toward the receiver, causing a DDM of open ocean [refer to Fig. 1(a)] to be more spread than the DDM of sea ice. Furthermore, in the marginal ice zone air–sea interaction is suppressed compared with open ocean conditions [31]. Consequently, the ice-covered surface will still appear smoother than open oceans given the same wind condition. Thus, the DDM over partially ice-covered area looks more spread than that of fully ice-covered but less spread than that of the open ocean. In summary, a spread DDM (or sliced input vector) will be associated with low SIC, and vice versa. It is obvious that the proposed method relies on the extent of spread in DDMs, which mainly varies with surface roughness that is dependent on SIC. By presenting the input DDM data along with desired SIC output, the NN for SIC retrieval was developed accordingly. For sea ice detection, another NN was established by using the input data and the ice detection target outcomes.

B. Test Results

The networks trained for ice detection and for concentration estimation were evaluated with data during another four collection periods (February 11–13 and 19–21, March 15–17, and April 16–18, 2015). The employed DDM data are listed in Table I. For sea ice detection application, the NN-based results have also been compared with the DDM observable-based [14] outcomes using the same DDM data. The sea ice detection results are tabulated in Table II. Comparison demonstrated superior accuracy of the NN-based method to the method in [14] for all five datasets.

To assess the SIC estimation, NN-based SIC results (SIC_{nn}) are compared with the same-day reference SIC data (SIC_{ref}). The mean error E_{av} , the mean absolute error E_{abs} , the standard deviation error E_{std} , and the correlation coefficient R between SIC_{nn} and SIC_{ref} are employed for evaluation purposes and they are given by

$$\begin{aligned}
 E_{av} &= \text{mean}(SIC_{nn} - SIC_{ref}) \\
 E_{abs} &= \text{mean}(|SIC_{nn} - SIC_{ref}|) \\
 E_{std} &= \text{std}(SIC_{nn} - SIC_{ref}) \\
 R &= \frac{\text{cov}(SIC_{nn}, SIC_{ref})}{\text{std}(SIC_{nn})\text{std}(SIC_{ref})}. \quad (6)
 \end{aligned}$$

The (normalized) error statistics for the SIC estimation are also given in Table II, from which low discrepancy between SIC_{nn} and SIC_{ref} is noticed for both training and test data. Insignificant degradation in accuracy between the test and training data suggests this method as a general application that can produce reliable estimation for the unseen data. The input vectors, outputs, and the ground-truth data for the test sets are shown in Fig. 6, in a sample by sample manner. It is clear that a spread input slice usually corresponds to a low SIC value. Furthermore, the estimated SIC is generally in accordance with the reference SIC. Based on the data analyzed here, the minimum detectable nonzero SIC is found to be 5%.

For demonstration, the SIC estimates from all employed DDMs are shown in a geographic frame in Fig. 7(a). Fig. 7(b) presents the collocated monthly SIC ground-truth data for reference. In addition, positions without DDM estimates were set as −40 following Fig. 2. Overall good agreement can be observed between the DDM-based SIC estimates and the ground-truth data. Despite this, some discrepancy can be noted around (15000) km, where both sea ice and seawater exists. Such ice-like reflections may be due to very calm water with low wind

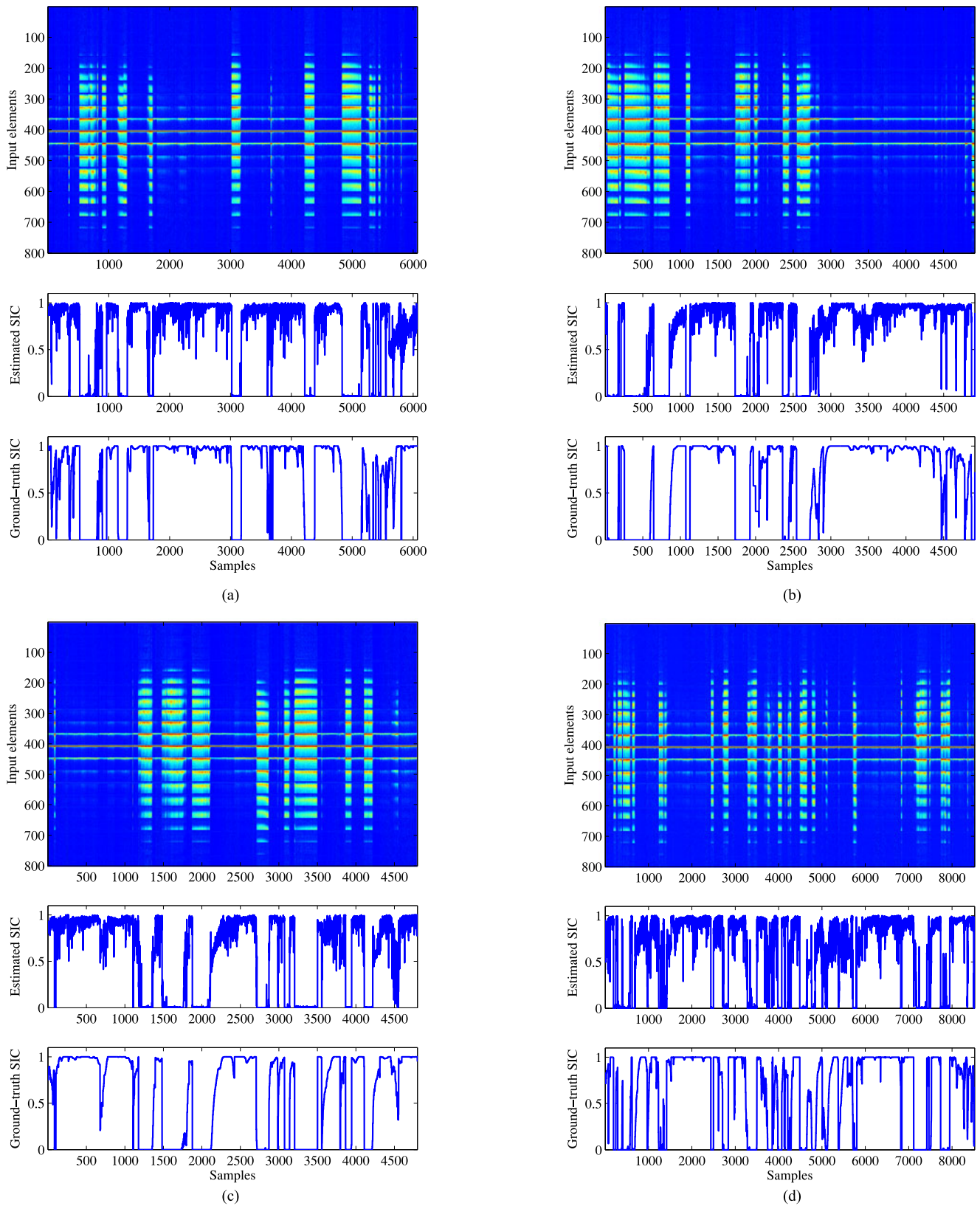
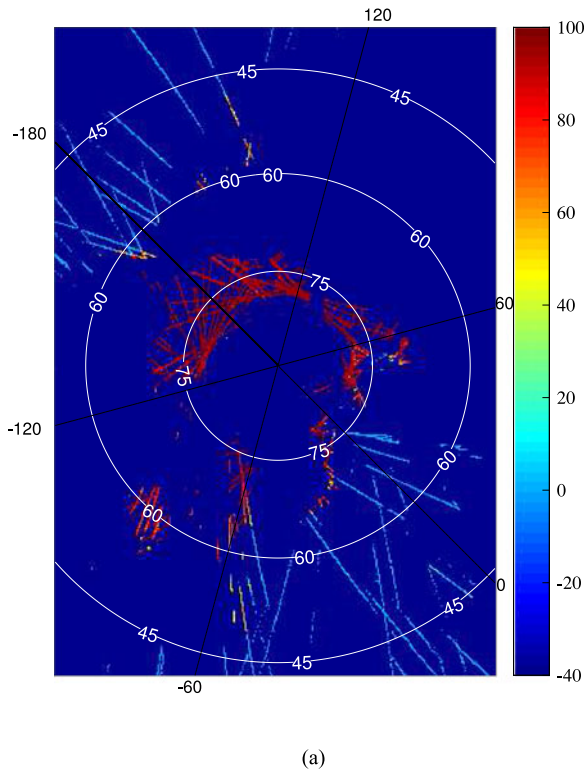
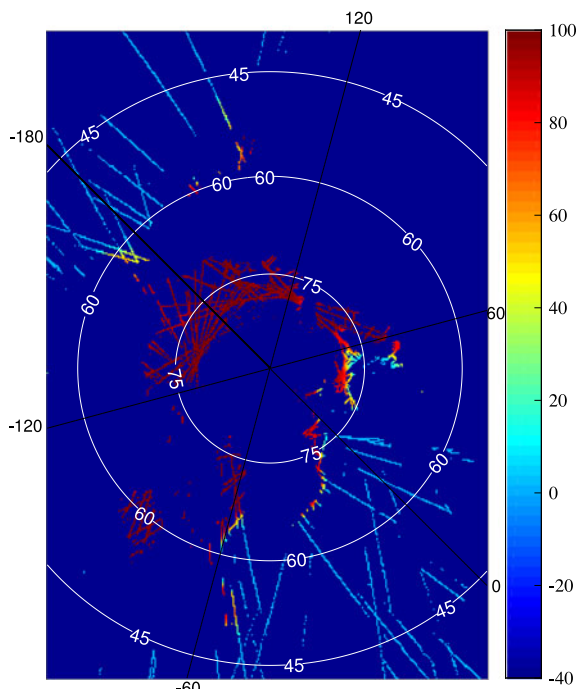


Fig. 6. SIC estimation using test data (with collection period): (a) RD 18 (February 11–13, 2015), (b) RD 19 (February 19–21, 2015), (c) RD 23 (March 15–17, 2015), and (d) RD 27 (April 16–18, 2015).



(a)



(b)

Fig. 7. SIC results: (a) average of estimation from datasets collected in February, 2015 and (b) corresponding colocated monthly ground-truth.

[14]. In order to further investigate this, the in situ measurement data of significant wave height (SWH) and wind speed (WS) from the National Data Buoy Center (NDBC) [32] were used for reference. Due to limited sea state data in the region under investigation, the DDMs collected on July 22, 2015 near

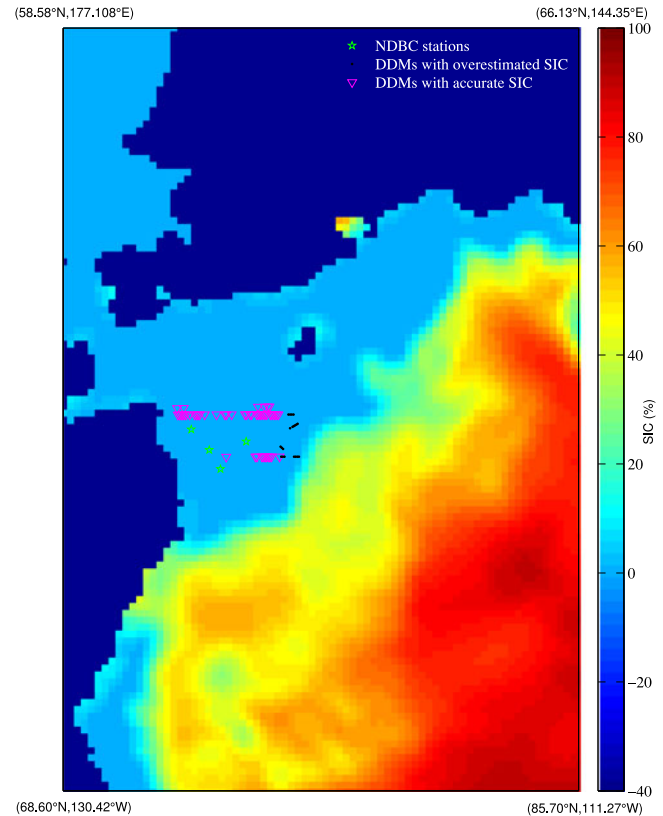


Fig. 8. Locations of NDBC stations and the SPs of the DDMs used for analyzing the effect of low sea state on SIC estimation. Green stars represent buoy stations. Black dots indicate the locations of DDMs resulting in overestimated SIC, whereas the magenta triangles depict those with accurate estimation. The background reference SIC data of July 22, 2015 were also from [21].

(within the distance of 200 km) the NDBC Stations 48012 (70.025°N , 166.071°W), 48214 (70.872°N , 165.248°W), 48213 (71.502°N , 164.133°W), and 48216 (71.502°N , 164.133°W) within the same period were analyzed. The SWH and WS data from the buoy station closest to each selected DDM and at the most immediate instant to the DDM collection time were used. The locations of the buoy stations and the selected DDMs are shown in Fig. 8. Furthermore, the SPs with overestimated SIC (15% higher than the reference SIC, which were about 0) are indicated by black dots, and those with precise results are depicted by magenta triangles. It can be noticed that overestimates mainly appear near the ice edge and this may account for the above-mentioned discrepancy in Fig. 7. The estimated and reference SICs as well as the corresponding SWH and WS are shown in Fig. 9 in terms of the distance from the associated DDM location to the closest ice edge. A slight sea state can be noticed for all the data analyzed in Fig. 9. Moreover, an average overestimation of 66% mainly occurred at the SP locations within 150 km from the ice edge. Otherwise, accurate results with an overall discrepancy of 1% can be obtained. Therefore, it may be inferred that the SIC tends to be overestimated at the regions near ice edge or partially ice-covered when the sea state and WS are low (even if it is not low, air-sea interaction is still suppressed). Such phenomenon can be noticed from the patterns around 3000 in the training set [see Fig. 5(b) and (c)] as well as

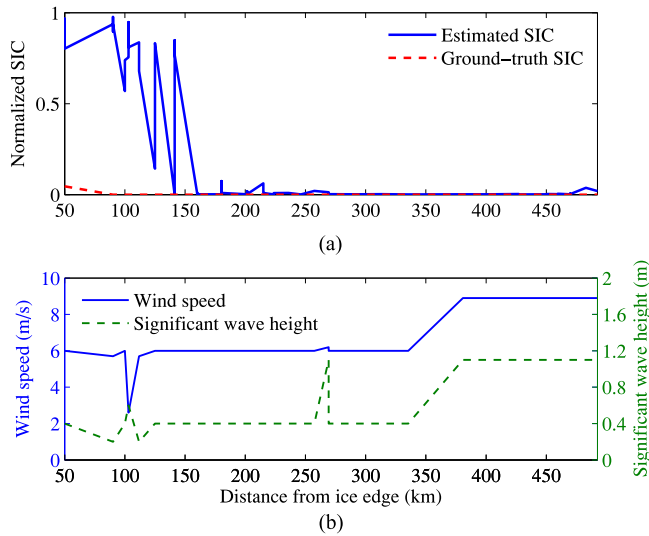


Fig. 9. Results under low sea state: (a) estimated and reference SICs and (b) SWH and WS data.

the patterns near 600 in Fig. 6(a), 600 in Fig. 6(b), and 3300 in Fig. 6(d) for the test sets.

On the other hand, underestimation also existed when the actual SIC was 100%. This might be caused by sea surface with ice of thickness larger than penetration depth. In this case, the scattering would be dominated by the uppermost sea ice, which could be rougher than the ice–water interface. In addition, if a DDM is contaminated by speckle noise at the nonspecular delay-Doppler bins, the SIC could also be underestimated. The cases of underestimation can be observed in Fig. 5(b) and (c) around the 2000th pattern for training set as well as the patterns around 6000 in Fig. 6(a), 1500 in Fig. 6(b), 2500 in Fig. 6(c), and 2000 in Fig. 6(d) for the test data.

V. CONCLUSION

In this paper, the feasibility of NN-based sea ice remote sensing (sea ice detection and SIC retrieval) from spaceborne GNSS-R DDMs is illustrated for the first time, using the TDS-1 data. An MLP (800 inputs, 1 hidden layer with 3 neurons, and 1 output) NN with LM algorithm based back-propagation learning is used. The training data are DDM pixels and the averaged SIC values from ground-truth. The averaging ensures the comparable spatial resolution between the DDM data and the SIC data.

Evaluation with ground-truth data confirms the performance of the proposed scheme. For the sea ice detection task, this approach shows improved accuracy compared with the observable-based method [14]. In particular, it is the first application of SIC estimation from DDMs. High accuracy has been obtained in both sea ice detection and concentration estimation through evaluation.

While this method holds great potential, further testing with more DDM data is necessary. In addition, it was found that the performance dropped for the partially ice-covered area, for which DDMs also depends on sea surface wind conditions. Therefore, it is worth investigating the scattering properties of GNSS-R signals for such regions. In particular, the DDMs

collected near ice edge with calm sea and low WS appear to give rise to overestimated SIC and false alarm. However, a further quantified analysis of the effect of low sea state on the SIC estimation should be achieved in the future with more in situ sea state data and DDM data. Although the adopted resolution matching scheme can provide reasonable comparison between DDMs and SIC data, it cannot provide the details about spatial coverage and its distribution of a DDM. It may be meaningful to consider precise spatial distribution of each DDM in the future. The dry/wet ice conditions may affect the performance of the SIC estimation. It has been reported in [33] that the melt water can lead to multiple contrast reversals on sea ice microwave signatures for different ice stages and seasons. However, due to lack of the dry/wet ice condition data, its effect on the detection performance cannot be evaluated in this paper. This problem will be investigated once such data become available. Dependence of the SIC estimation on ice thickness will also be studied. Last, this work may open a window for more DDM-based remote sensing application with NN in the future.

ACKNOWLEDGMENT

The authors are grateful to the TDS-1 team for the work of making the GNSS-R DDM data available.

REFERENCES

- [1] R. G. Barry, M. C. Serreze, J. A. Maslanik, and R. H. Preller, "The Arctic sea ice-climate system: Observations and modeling," *Rev. Geophys.*, vol. 31, no. 4, pp. 397–422, Nov. 1993.
- [2] R. J. Galley, B. G. T. Else, S. J. Prinsenberg, D. Babb, and D. G. Barber, "Summer sea ice concentration, motion, and thickness near areas of proposed offshore oil and gas development in the Canadian Beaufort Sea-2009," *Arctic*, vol. 66, no. 1, pp. 105–116, Mar. 2013.
- [3] M. Hamer, "The polar road to riches," *New Sci.*, vol. 189, no. 2535, pp. 24–25, Jan. 2006.
- [4] D. K. Hall and J. Martinec, *Remote Sensing of Ice and Snow*. London, U.K.: Chapman & Hall, 1985.
- [5] G. I. Belchansky and D. C. Douglas, "Classification methods for monitoring Arctic sea-ice using OKEAN passive/active two-channel microwave data," *J. Remote Sens. Environ.*, vol. 73, no. 3, pp. 307–322, Sep. 2000.
- [6] A. Komjathy, J. Maslanik, V. U. Zavorotny, P. Axelrad, and S. J. Katzberg, "Sea ice remote sensing using surface reflected GPS signals," in *Proc. IEEE Int. Geosci. Remote Sens. Symp.*, Jul. 2000, pp. 2855–2857.
- [7] Y. Zhang *et al.*, "Detection of Bohai Bay sea ice using GPS-reflected signals," *IEEE J. Sel. Topics Appl. Earth Observ. Remote Sens.*, vol. 8, no. 1, pp. 39–46, Jan. 2015.
- [8] F. Fabra *et al.*, "Monitoring sea-ice and dry snow with GNSS reflections," in *Proc. IEEE Int. Geosci. Remote Sens. Symp.*, Jul. 2010, pp. 3837–3840.
- [9] M. B. Rivas, J. A. Maslanik, and P. Axelrad, "Bistatic scattering of GPS signals off Arctic sea ice," *IEEE Trans. Geosci. Remote Sens.*, vol. 48, no. 3, pp. 1548–1553, Mar. 2010.
- [10] S. Gleason, "Towards sea ice remote sensing with space detected GPS signals: Demonstration of technical feasibility and initial consistency check using low resolution sea ice information," *Remote Sens.*, vol. 2, no. 8, pp. 2017–2039, Aug. 2010.
- [11] J. Tye, P. Jales, and M. Unwin, "Ice sensing with the TDS-1 SGR-ReSI," presented at the *8th Workshop GNSS Reflectometry*, Potsdam, Germany, 2015.
- [12] L. Peraza *et al.*, "GNSS-R sea-ice characterization: Preliminary results from UK-TDS-1 low Earth orbiter," presented at the *8th Workshop GNSS Reflectometry*, Potsdam, Germany, 2015.
- [13] Q. Yan and W. Huang, "Sea ice detection from GNSS-R delay-Doppler map," in *Proc. 17th Int. Symp. Antenna Technol. Appl. Electromagn.*, Montreal, QC, Canada, Jul. 2016, pp. 1–2.
- [14] Q. Yan and W. Huang, "Spaceborne GNSS-R sea ice detection using delay-Doppler maps: First results from the UK TechDemoSat-1 Mission," *IEEE J. Sel. Topics Appl. Earth Observ. Remote Sens.*, vol. 9, no. 10, pp. 4795–4801, Oct. 2016.

- [15] A. AlonsoArroyo, V. U. Zavorotny, and A. Camps, "Sea ice detection using GNSS-R data from UK TDS-1," in *Proc. IEEE Int. Geosci. Remote Sens. Symp.*, Beijing, China, Jul. 2016, pp. 2001–2004.
- [16] R. H. Nielsen, "Kolmogorov's mapping neural network existence theorem," in *Proc. IEEE Int. Conf. Neural Netw.*, New York, NY, USA, 1987, pp. 11–13.
- [17] L. Wang, K. A. Scott, L. Xu, and D. A. Clausi, "Sea ice concentration estimation during melt from dual-pol SAR scenes using deep convolutional neural networks: A case study," *IEEE Trans. Geosci. Remote Sens.*, vol. 54, no. 8, pp. 4524–4533, Aug. 2016.
- [18] L. P. Bobylev, E. V. Zabolotskikh, L. M. Mitnik, and O. M. Johannessenn, "Neural-network based algorithm for ice concentration retrievals from satellite passive microwave data," in *Proc. MICRORAD 2008*, Firenze, Italy, 2008, pp. 1–4.
- [19] G. Foti *et al.*, "Spaceborne GNSS reflectometry for ocean winds: First results from the UK TechDemoSat-1 mission," *Geophys. Res. Lett.*, vol. 42, no. 13, pp. 5435–5441, Jul. 2015.
- [20] M. P. Clarizia, C. Ruf, P. Cipollini, and C. Zuffada, "First spaceborne observation of sea surface height using GPS-reflectometry," *Geophys. Res. Lett.*, vol. 43, no. 2, pp. 767–774, Jan. 2016.
- [21] D. J. Cavalieri, C. Parkinson, P. Gloersen, and H. J. Zwally, "Sea ice concentrations from Nimbus-7 SMMR and DMSP SSM/I passive microwave data," Nat. Snow Ice Data Center, Boulder, CO, USA, 1996.
- [22] S. Haykin, *Neural Networks: A Comprehensive Foundation*, 2nd ed. Upper Saddle River, NJ, USA: Prentice-Hall, 1999.
- [23] "All about sea ice, "Data: Terminology"," Nat. Snow Ice Data Center, 2016. [Online]. Available: <https://nsidc.org/cryosphere/seaice/data/terminology.html>
- [24] K. Hornik, M. Stinchcombe, and H. White, "Multilayer feedforward networks are universal approximators," *Neural Netw.*, vol. 2, pp. 359–366, 1989.
- [25] P. Werbos, "Beyond regression: New tools for prediction and analysis in the behavioral sciences," Ph.D. dissertation, Committee on Appl. Math., Harvard Univ., Cambridge, MA, Nov. 1974.
- [26] D. W. Marquardt, "An algorithm for least-squares estimation of nonlinear parameters," *J. Soc. Ind. Appl. Math.*, vol. 11, no. 2, pp. 431–441, Jun. 1963.
- [27] M. T. Hagan and M. Henhaj, "Training feedforward networks with the Marquardt algorithm," *IEEE Trans. Neural Netw.*, vol. 5, pp. 989–993, 1994.
- [28] H. Yu and B. M. Wilamowski, "Levenberg-Marquardt training," in *Industrial Electronics Handbook-Intelligent Systems*, vol. 5. Boca Raton, FL, USA: CRC Press, 2011, pp. 12–1—12–15.
- [29] G. Heygster *et al.*, "L-band radiometry for sea-ice applications," Inst. Environ. Phys., Univ. Bremen, Bremen, Germany, *Tech. Rep. Final Report for ESA/ESTEC Contract No. 21130/08/NL/EL*, 2009.
- [30] M. L. Bryan and R. W. Larson, "The study of freshwater lake ice using multiplexed imaging radar," *J. Glaciol.*, vol. 14, no. 72, pp. 445–457, 1975.
- [31] S. Zippel and J. Thomson, "Air-sea interactions in the marginal ice zone," *Elementa Sci. Anthropocene*, no. 4, vol. 95, 2016. [Online]. Available: <http://doi.org/10.12952/journal.elementa.000095>
- [32] National Data Buoy Center. 2015. [Online]. Available: <http://www.ndbc.noaa.gov>
- [33] R. G. Onstott, T. C. Grenfell, C. Matzler, C. A. Luther, and E. A. Svendsen, "Evolution of microwave sea ice signatures during early summer and midsummer in the marginal ice zone," *J. Geophys. Res.*, vol. 92, no. C7, pp. 6825–6835, Jun. 1987.



Qingyun Yan (S'14) was born in Haimen, China. He received the B.Eng. degree in electronic science and engineering from the Nanjing University of Posts and Telecommunications, Nanjing, China, in 2014, and the M.Eng. degree in electrical engineering in 2015 from the Memorial University of Newfoundland, St. John's, NL, Canada, where he is currently working toward the Ph.D. degree in electrical engineering.

His research interests include tsunami detection and sea ice remote sensing using global navigation satellite system-reflectometry.



Weimin Huang (M'10–SM'13) received the B.S., M.S., and Ph.D. degrees in radio physics from Wuhan University, Wuhan, China, in 1995, 1997, and 2001, respectively. He received the M.Eng. degree and a Postdoctoral Fellowship in engineering electromagnetics from Memorial University, St. John's, NF, Canada.

From 2008 to 2010, he was a Design Engineer at Rutter Technologies. Since 2010, he has been with the Faculty of Engineering and Applied Science, Memorial University, where he is currently an Associate Professor. His past and present research interest involves the mapping of oceanic surface parameters via high-frequency ground wave radar, X-band marine radar and, more recently, global navigation satellite systems.

Dr. Huang is an Associate Editor for the IEEE ACCESS and an editorial member of the *Remote Sensing*.



Cecilia Moloney (M'91) received the B.Sc. (Hons.) degree in mathematics from the Memorial University of Newfoundland, St. John's, NL, Canada, in 1978, and the M.A.Sc. and Ph.D. degrees in systems design engineering from the University of Waterloo, Waterloo, ON, Canada, in 1980 and 1988, respectively.

From 2004 to 2009, she held the NSERC/Petro-Canada Chair for Women in Science and Engineering, Atlantic Region. Since 1990, she has been a faculty member with the Memorial University of Newfoundland, where she is currently a Full Professor of electrical and computer engineering. Her research interests include nonlinear signal- and image-processing methods, signal representations via wavelet and contourlet transforms, radar signal processing, transformative pedagogy for science and engineering, and gender and science studies.